
**Liquid Crystals**
Publication details, including instructions for authors and subscription information:
http://www.informaworld.com/smpp/title~content=t713926090

# Pattern formation and non-linear phenomena in stretched discotic liquid crystal fibres

L. Wang; A. D. Rey

Online publication date: 06 August 2010

**To cite this Article** Wang, L. and Rey, A. D.(1997) 'Pattern formation and non-linear phenomena in stretched discotic liquid crystal fibres', Liquid Crystals, 23: 1, 93 — 111
**To link to this Article: DOI:** 10.1080/026782997208712
**URL:** http://dx.doi.org/10.1080/026782997208712

LIQUID CRYSTALS, 1997, VOL. 23, NO. 1, 93–111

# Pattern formation and non-linear phenomena in stretched discotic liquid crystal fibres

by L. WANG† and A. D. REY*‡

†Department of Mathematics and Statistics, McGill University, 805 Sherbrooke Str. W., Montreal, PQ H3A 2K6, Canada

‡Department of Chemical Engineering, McGill University, 3480 University Str., Montreal, PQ H3A 2A7, Canada

(*Received 24 January 1997*)

This paper presents a non-linear numerical and bifurcation analysis of pattern formation phenomena in a discotic nematic liquid crystal confined to annular cylindrical cavities and subjected to extensional deformations. The results are of direct relevance to understanding the industrial melt spinning of mesophase carbon fibres, using discotic nematic liquid crystals precursor materials. Three types of orientation patterns are identified in this study: spatially constant (radial), monotonic (pinwheel), and oscillatory (zigzag). Numerical and closed form analytical results predicting continuous transformations between the radial, pinwheel, zigzag radial orientation modes are presented. The bifurcation analysis provides a direct characterization of the parametric dependence and the transitions between these three basic patterns, and provides a complete understanding of the multistability phenomena that is present in the oscillatory orientation patterns. In general it is found that small fibres of nearly elastically isotropic discotic nematic liquid crystals tend to adopt the classical ideal radial texture, while larger fibres with anisotropic elastic moduli tend to yield the zigzag texture. Fixed arbitrary surface orientation of intermediate size and anisotropy tend to adopt the pinwheel texture. The theoretical results are able to explain the main features and mechanisms that lead to the commonly observed cross-section textures of industrially spun mesophase carbon fibres.



## 1. Introduction

The industrial fabrication of mesophase carbon fibres [1–3] is based on the melt spinning of discotic nematic liquid crystals into micron-sized cylindrical filaments. As in other man-made organic fibres molecular orientation is a key parameter that dominates the mechanical property profile. For disk-like molecules the distinguishing molecular direction is the unit normal to the molecular disks, and the average orientation characteristic of nematic ordering arises from the close alignment of the molecular unit normals. During fibre spinning, a uniaxial extensional stretching flow orients the longest molecular dimension of the disk-like molecules close to the extension (flow direction), such that the average molecular orientation is normal to this direction, and contained in the plane normal to the fibre axis. Thus any spun mesophase fibre cross-section displays a planar orientation. A variety of planar orientation patterns have been frequently reported in the literature, including the onion, radial, and zigzag radial patterns, shown in figure 1 [4]. The patterns shown contain a line defect along the fibre axis, while the surface orientation is planar for the onion pattern, homeotropic for the radial, and arbitrary for the zigzag. It should be noted that in actual fibres the defect gives rise to a macroscopic isotropic core, apparently much larger than the typical molecular size of nematic disclinations [5]. The radial zigzag pattern observed in actual fibres [6] has a position dependent amplitude and wavelength but the basic textural feature of interest is the radially oscillatory trajectories of the molecular planes.

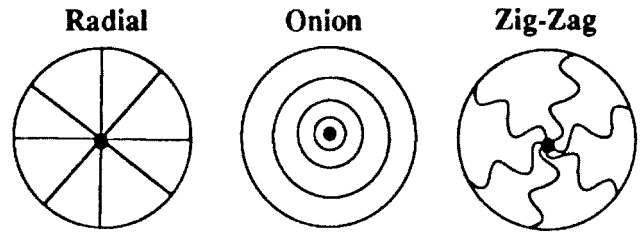


Figure 1. Schematic representation of the average molecular trajectories in the cross-section of mesophase fibres observed during industrial spinning process (see Pencock [6], Peebles [7] for more details). The lines here represent the curves orthogonal to the average molecular orientation (director), defined in figure 2, and are thus tangent to the planar disk-like molecules.

*Author for correspondence.

0267–8292/97 $12·00 

The selection mechanisms that drive the pattern formation in mesophase fibres spun from discotic nematic liquid crystals are at present not well understood, but due to strong structure–properties correlations they are essential for product optimization. On the other hand, the closely related problem of pattern formation in cylindrical cavities filled with rod-like nematics is better understood [7, 8]. In the latter case, theoretical predictions using energy minimizing models, are able to reproduce many observed patterns. Below we show that similar elastic minimization mechanisms are able to explain the pattern formation phenomena in discotic nematic filaments subjected to ideal extensional flows.

Previous work [9] on pattern formation in confined discotic nematic liquid crystals mainly focused on predictions of the radial and radial zigzag patterns, using a simplified linear analysis. The analysis predicted that oscillatory pattern arises due to the anisotropy that characterizes the planar elastic deformation modes, but only if the outer boundary conditions are not homeotropic. Thus the only transformation leading to a zigzag pattern involves a bifurcation of the pinwheel pattern, also known as the magic spiral [5], in which the molecular trajectories follow a pinwheel pattern (see figure 4). This is obviously in disagreement with experiments [6], where the surface orientation can be arbitrary and in fact it is ill-defined [6]. In addition, the linear analysis of [9] is only valid for small director distortions, and it also predicts unbounded oscillations for certain critical values of the fibre radius, which is again unphysical. The above shortcomings indicate an incomplete knowledge of what parameter envelopes lead to specific patterns in stretched discotic nematic liquid crystal filaments. To develop a complete picture of pattern formation in confined discotic nematic liquid crystals here we focus on orientation patterns that arise from all possible continuous transformations of the ideal radial pattern, in which the molecular disks follow radial trajectories (see figure 4). In addition since the isotropic cores found along the fibre axis are in practice of macroscopic size, we study confinement in an annular geometry [6].

For rod-like liquid crystals, previous work on planar textures of confined nematics in cylindrical cavities [10] proved the existence of spatially oscillatory solutions to the equilibrium equation, and also established the stability properties of the solutions. In [10] it is predicted the existence of an infinite number of oscillatory solutions for homeotropic boundary conditions when the two relevant splay–bend elastic constants are different, which in general disagrees with the multiple bifurcation and multistability phenomena in cylindrical confined geometries as shown below. Analysis of the linearized model for confined rod-like nematics in cylindrical cavities [11] shows oscillatory solutions for non-homeotropic boundary conditions. However, due to the shortcomings of linearization, the bifurcation and multistability phenomena, due to non-linearity of the elastic free energy model, remained unexplored. In this paper, we overcome the above mentioned shortcomings of previous works and give a complete analysis of planar textures of confined nematics in cylindrical cavities. Non-planar pattern formation as well as planar pattern formation with off-axis singularities in rod-like nematics confined to cylindrical cavities have also been characterized using energy minimization model [12]. Nevertheless these works do not consider the planar patterns studied here.

The objective of this paper is: (1) to reproduce and explain the main pattern formation phenomena that are observed during the spinning of carbonaceous mesophase using well established liquid crystal elasticity models; (2) to provide a comprehensive characterization of planar orientation patterns of discotic nematics liquid crystals subjected to flow; and (3) to establish the main bifurcational and non-linear phenomena present in discotic nematics in cylindrical cavities.

This paper is organized as follows. §2 deals with the elastic modes of discotic nematics, and discusses the elastic anisotropies in planar orientation patterns. §3 presents the mathematical model that describes steady state planar orientation patterns in cylindrical cavities in the presence of fixed boundary conditions. Equations that validate the planarity assumption in the presence of extensional (fibre spinning) flow are presented. §4 presents the numerical results and discussion. The results are organized and classified along the values of the governing parameters. Closed form bifurcation thresholds, bifurcation diagrams, and stability diagrams are presented. A summary of the main features of the pattern formation phenomena is also included.

## 2. Elastic modes of discotic nematics liquid crystals

In this section we describe the main features of nematic elasticity for discotic nematics in cylindrical cavities displaying planar (2D) textures, and use them to identify the elastic modes in typical mesophase carbon fibre textures. Figure 2 shows the molecular geometry, positional disorder, and uniaxial orientational order of the model uniaxial discotic nematic liquid crystal considered in this paper [5]. The partial orientational ordering of the molecular unit normals $\mathbf{u}$ is along the average orientation or director $\mathbf{n}$ ($\mathbf{n}\ \mathbf{n} = 1$), and differs from that of rod-like molecules in that $\mathbf{u}$ is along the shortest molecular dimension. This geometric difference is the source of the reversal in the ordering of viscoelastic [13, 14] as well as other properties [2], that arise when comparing disk-like and rod-like uniaxial nematics. This

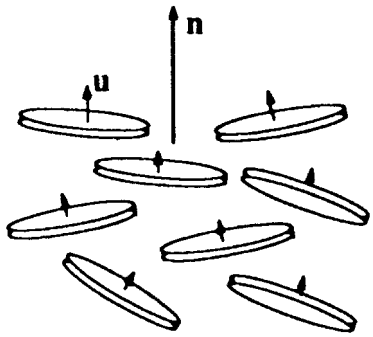


Figure 2. Orientational ordering in the uniaxial discotic nematic phase. The molecular normals **u** of the randomly positioned disk-like molecules, partially orient along the director **n**.

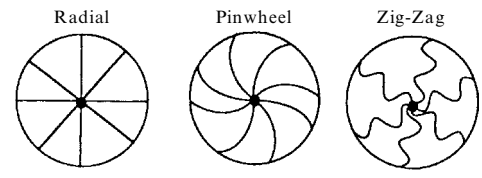


| | | | |
|---|---|---|---|
| Orientation ($\theta(r)$) | constant | monotonic | periodic |
| Characteristics | $\theta = \pi/2$ | sign$\{\theta''\} \equiv$ const. | $\theta(\ln r) = \theta(\ln r + \lambda)$ |
| Outer BC | $\theta_o = \pi/2$ | $\theta_o \neq \pi/2$ | chiral $\theta_o \neq \pi/2$ |
| | | | achiral $\theta_o = \pi/2$ |
| Deformation | bend | splay-bend | splay-bend |

Figure 4. Schematics of a planar radial pattern (PR), the planar pinwheel pattern (PPW), and the planar zigzag radial pattern (PZRi; i = h: homeotropic, i = n: non-homeotropic). The text below the schematics summarizes the main features of each pattern.

paper is restricted to the study of planar patterns, containing splay and bend deformation [5]. Figure 3 shows the splay mode of modulus $K_1$, and the bend mode of modulus $K_3$. Note that in contrast to rod-like nematics, for disk-like nematics the bending disks trajectories give rise to splay deformation (left figure), and the splaying disks trajectories give rise to bend deformation (right figure); by disk trajectory we mean the curve locally orthogonal to the director. Using a circular cylindrical coordinate system $(r, \psi, z)$, the $z$-coordinate is along the fibre axis, and the transverse plane is spanned by the azimuthal direction of $(\psi)$ and the radial $(r)$ direction; here $0 \leqslant \psi \leqslant 2\pi$ and $r_c \leqslant r \leqslant r_o$, where $r_c$ is the isotropic core radius, and $r_o$ is the outer radius which for typical mesophase carbon fibres is in the micron size range. In this cylindrical geometry, the stationary radially dependent planar director field of figure 1 can be parametrized as $\mathbf{n}(r) = (n_r, n_\psi, n_z) = (\cos\theta, \sin\theta, 0)$; here $n_z = 0$ means planar orientation and absence of twist deformations [5]. Figure 4 shows schematics of a radial transverse texture (left) and a radial zigzag texture (right), typically oberved in mesophase carbon fibres [4, 6]. The full lines indicate the disks trajectories, which are locally orthogonal to the directors. Based on our previous discussion, it follows that the radial texture of a uniaxial discotic nematic, defined by $n_\psi(r) = 1$ and $r_c \leqslant r \leqslant r_o$, contains a pure bend mode. On the other hand, a radial zigzag texture consists of a mixed splay–bend deformation mode, and in addition $n_\psi(1) \neq 1$. A comparison of the two schematics shown in figure 4 indicates that if the radial zigzag texture is selected over the pure radial texture then the trade-off of bend by splay in the oscillatory pattern must be energetically favourable, as quantitatively shown below.

For low molar mass discotic nematics, theory [13] and experiment [15] show that $K_1 > K_3$. An increase in the molecular weight of disk-like nematics, just as for

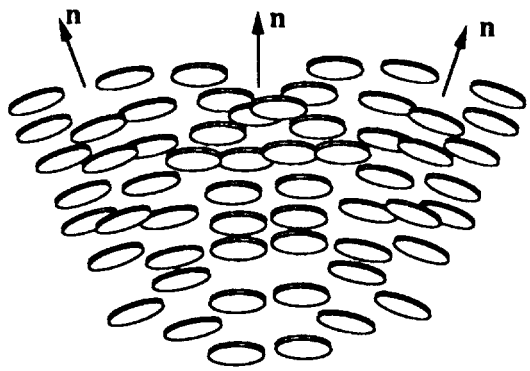


SPLAY MODE ( $K_1$ )

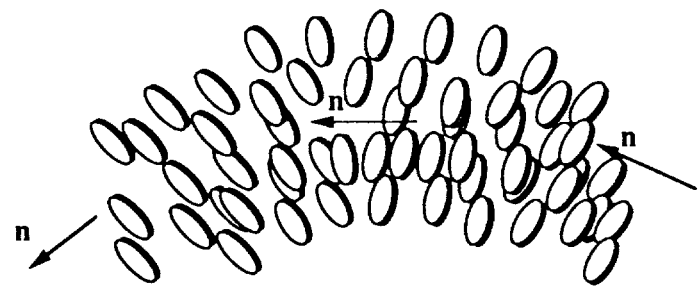


BEND MODE ( $K_3$ )

Figure 3. Schematics of the elastic splay deformation (left) and bend deformation (right) for uniaxial discotic nematics. Note that the splay (bend) mode involves bending (splaying) of the disks trajectories, in contrast to the case of uniaxial rod-like nematics. A disk trajectory is a curve locally orthogonal to the director.

rod-like nematics [16], can be expected to reverse the ordering of the elastic constants, so that for higher molecular weight discotic nematics, like carbonaceous mesophases, we can expect $K_3 > K_1$. Thus, just as polymeric rods avoid the splay of the radial texture by introducing director oscillations [10, 11], polymeric disks avoid the bend of the radial texture of a zigzagging director field [9].

## 3. Governing equations

To establish the origin of planar orientation textures we first discuss the effect of an external extensional flow in the $z$-direction on the texture formation in the $\psi - r$ plane. The non-zero components of the rate of deformation tensor $A_{ij}$ for an extensional flow are [17]: $A_{zz} = -A_{rr} = \dot{\varepsilon}$, where $\dot{\varepsilon}$ is the extension rate, and the vorticity tensor for this irrotational flow is $\mathbf{W} = 0$. At steady state, the viscous torques $\Gamma^{\upsilon}$ acting on the director are $\Gamma^{\upsilon} = -\mathbf{n} \times (\gamma_2 \mathbf{A}\ \mathbf{n})$, where the $\gamma_2$ is a torque coefficient [5]. As is well known [18], in this flow the stable director orientation is normal to the extension direction (i.e. transverse $\psi - r$ plane), and therefore $\Gamma^{\upsilon} = 0$. Thus the net effect of the extensional flow on the texture formation is to keep the director in the $\psi - r$ transverse plane. Therefore, we may conclude that, given sufficient long process times as compared to reorientation times, the transverse radial zigzag pattern is selected by the minimization of the splay–bend elastic free energy per unit fibre length. If the inequality in the time scales does not hold, the assumption of planarity does not generally hold. In actual typical fibre spinning process there is ample evidence that shows that the process time is greater than the director reorientation time, so that the planar orientation assumption is realistic, and always observed [4, 6].

Since the viscous torques $\Gamma^{\upsilon}$ due to the extensional flow acting on the director $\mathbf{n}$ vanish with planar orientation ($n_z = 0$), the selection of the pattern is just dictated by a minimization of the Frank [5] elastic energy due to, at most, splay and bend modes. The equilibrium equation for the director of discotic nematic liquid crystals is derived from the extremum condition of the free energy. Since there are no twist deformations in planar orientation, the Frank elastic energy density reduces to [5]:

$$f = \frac{1}{2}\{K_1(\nabla\ \mathbf{n})^2 + K_3(\mathbf{n} + \nabla \times \mathbf{n})^2\} \tag{1}$$

where $\mathbf{n}$ is the director. Note that saddle–splay elasticity ($K_{12}$) plays no role in planar patterns. Thus the total free energy is given by

$$F = \int_{\Omega} f \, \mathrm{d}\upsilon \tag{2}$$

where $\Omega$ is the total volume. Expressing the director $\mathbf{n}$ in terms of independent variables $q_i$, and taking the first variation of the total free energy integral, we obtain the Euler–Lagrange equilibrium equation:

$$\frac{\delta F}{\delta \mathbf{n}} = \frac{\partial f}{\partial \mathbf{n}} - \nabla\ \frac{\partial f}{\partial \mathbf{n}'} = 0 \tag{3}$$

where $\nabla = \partial/\partial q_i$ and $\mathbf{n}' = \partial \mathbf{n}/\partial q_i$. We assume that the pattern is rotationally symmetric in the cross-section $\psi - r$ plane, such that the director $\mathbf{n}$ would be only a function of the radial distance ($r$) from the axis of rotational symmetry. The total free energy is

$$F = \int_L F_{2d} \, \mathrm{d}r \tag{4}$$

where

$$F_{2\mathrm{d}} = 2\pi \int_{R_\mathrm{c}}^{R_\mathrm{o}} fr \, \mathrm{d}r = 2\pi \int_{u_\mathrm{c}}^{u_\mathrm{o}} f\left(\mathbf{n}, \frac{\mathrm{d}\mathbf{n}}{\mathrm{d}u}, u\right) \mathrm{d}u \tag{5}$$

is the free energy per unit length, and $u = \ln(r/r_\mathrm{c})$. Equations (4) and (5) show that the numerical value of the total free energy per unit length depends on $f$. In polar coordinates, the director $\mathbf{n}$ is expressed by the polar angle $\phi$ as

$$\mathbf{n}(\phi) = (\cos\phi, \sin\phi, 0) \tag{6}$$

where $\phi$ is position dependent, $\phi = \phi(u)$, and the unit length restriction $\mathbf{n}\ \mathbf{n} = 1$ is satisfied. In terms of the generalized variable $u$, the equilibrium equation becomes

$$\frac{\partial f}{\partial \phi} - \frac{\mathrm{d}}{\mathrm{d}u}\frac{\partial f}{\partial \phi'} = 0 \tag{7}$$

where the prime denotes differentiation with respect to $u$. This is the governing equation in this analysis. Using the expression of $\mathbf{n}$ of (6) in (3), we have

$$f = \frac{K_1}{2}\{\cos^2\phi - 2\phi' \sin\phi\cos\phi + \phi'^2 \sin^2\phi\} + \frac{K_3}{2}\{\sin^2\phi + 2\phi' \sin\phi\cos\phi + \phi'^2\cos^2\phi\}. \tag{8}$$

Taking the variation of above expression of the free energy density, we obtain the equilibrium equation,

$$\sin\phi\cos\phi\{-K_1 + K_3\} + \sin\phi\cos\phi\{-K_1 + K_3\}\phi'^2 + \{-K_1\sin^2\phi - K_3\cos^2\phi\}\phi'' = 0. \tag{9}$$

Scaling with $K_3$ we get

$$\sin\phi\cos\phi\{(1-\mu)(1+\phi'^2)\} - \{\cos^2\phi + \mu\sin^2\phi\}\phi'' = 0 \tag{10}$$

where $\mu = K_1/K_3$. The boundary conditions studied here

are

$$u(0)=\frac{\pi}{2} \qquad \text{and} \qquad u(u_o)=\phi_o . \tag{11}$$

The solution to (10, 11) is $\phi(u)$ and the parameter vector is $p=(\mu, \phi(u_o), \Delta u)$. The deviation of $\mu$ from 1 denotes elastic anisotropy, the deviation of $\phi(u_o)$ from $\phi(0)$ introduces asymmetric boundary condtions, and $\Delta u$ is a scale of fibre size such that increasing (decreasing) $\Delta u$ represents smaller (larger) fibre cavities.

The equilibrium equation (10) is a non-linear second order ordinary differential equation. For symmetric boundary conditions of $\phi(0)=\phi(u_o)=\pi/2$ ($\phi(0)=\phi(u_o)=0$), the trivial solutions of $\phi=\pi/2$ ($\phi=0$) exist for all values of $\mu$. For asymmetric boundary conditions, i.e. $\phi(0)\neq\phi(1)$, previous work [9] has shown the existence of oscillatory solutions when the elastic constants are not equal ($\mu\neq 1$), using a linearized equilibrium equation. Here we complete this work, by carrying out a full analysis of the non-linear equation (10).

Given the possibility of multistability and solution multiplicities, generic in non-linear equations, we compute all equilibrium points of equation (9) using an efficient root finder based on the shooting method [19]. Briefly, we rewrite the governing equation (10) as two first order differential equations system:

$$\begin{aligned}\phi' &= \psi \\ \psi' &= \frac{(-\mu+1)\sin\phi\cos\phi(1+\psi^2)}{\mu\sin^2\phi+\cos^2\phi}.\end{aligned} \tag{12}$$

The boundary conditions are

$$\phi(0)=\frac{\pi}{2} \qquad \text{and} \qquad \psi(0)=p \tag{13}$$

where $p=\phi'(0)$ is a new parameter. By introducing the new parameter $p$, we consider the value of $\phi(u_o)$ as a function of $p$, once $\mu$ is fixed. We next perform a numerical study using a fourth order Ronge–Kutta method [19]. By solving for $p$ for a given value of $\phi(u_o)$, we are able to find all the stable as well as unstable solutions of equation (10). The numerical study identified all the solution branches and their parametric dependencies on the outer boundary condition $\phi(u_o)$, and elastic anisotropy $\mu$, for a given value of $u_o$).

## 4. Numerical results and discussions

The numerical solutions found in this study are naturally classified and characterized by the symmetry properties of the director field. Figure 4 summarizes the classifications of the three classes of planar patterns arising in discotic nematics in annular cylindrical cavities with surface orientation at the inner radius fixed at $\pi/2$. Below each descriptive name (radial, pinwheel, zigzag) we show a sketch of the orientation profiles, and the main signatures of each pattern. The planar radial (PR) pattern has a pure bend deformation and the outer boundary condition is homeotropic ($\phi(u_o)=\pi/2$). The planar pinwheel (PPW) pattern, also known as the magic spiral [5], has monotonic splay–bend deformations, and arise with non-homeotropic ($\phi(u_o)\neq\pi/2$) boundary conditions. The planar zigzag radial (PZRi) pattern has periodic splay–bend deformations and may occur with homeotropic (i = h) or non-homeotropic (i = n) outer boundary conditions. Figure 5 shows a block diagram that summarizes the transformation paths between the three orientation patterns. The figure shows that the radial pattern can be transformed into the pinwheel pattern by changing the outer surface orientation ($T_1$). The radial pattern can also be transformed into the homeotropic zigzag radial pattern (PZRh) by temperature changes (increase in elastic anisotropy) or by increasing the ratio between the outer and the inner radius ($\Delta u$). Similarly, the pinwheel (PPW) pattern can be transformed into a non-homeotropic zigzag radial pattern (PZRn) by the change in temperature and by increasing $\Delta u$. The transformation between homeotropic and non-homeotropic patterns are achieved by changing the outer surface orientations.

Figure 6 shows a summary of numerical simulation results of the orientation $\phi$(rad) as a function of dimensionless distance $u$, for $\Delta u=1$. These results summarize the $T_1$ and $T_2$ transformations. Starting with the top left, the panels towards the right correspond to increasing elastic anistropy ($\mu=K_1/K_3$) and the panels towards the bottom correspond to increasing values of outer cylinder surface orientation ($\phi(u_o)$). The orientation changes in the different panels of the figure clearly reflect the transformation paths shown in figure 5. Moving towards the left in the top row corresponds to the $T_2$ transformation of the radial pattern (PR) into the homeotropic zigzag radial pattern (PZRh). Moving towards the left in the middle and the bottom rows correspond to the $T_2$ transformation paths of planar pinwheel pattern (PPW) into non-homeotropic zigzag radial pattern (PZRn). Moving down corresponds to the $T_1$ transformation between (PR) and (PPW) patterns (left column), and also the $T_1$ transformation between (PZRh) and (PZRn) patterns (right column).

Figure 7 shows the corresponding summary of the $T_1$ and $T_3$ transformations. In figure 7 the elastic anisotropy is fixed at $\mu=0{\cdot}15$, and left column represents the patterns for $\Delta u=1$, while the right column represents the patterns for $\Delta u=3$. Moving from top to bottom in the left column corresponds to the $T_1$ transformation between (PR) and (PPW) pattern, and moving vertically on the right column corresponds to the $T_1$ transformation between (PZRh) and (PZRn) pattern. Moving on

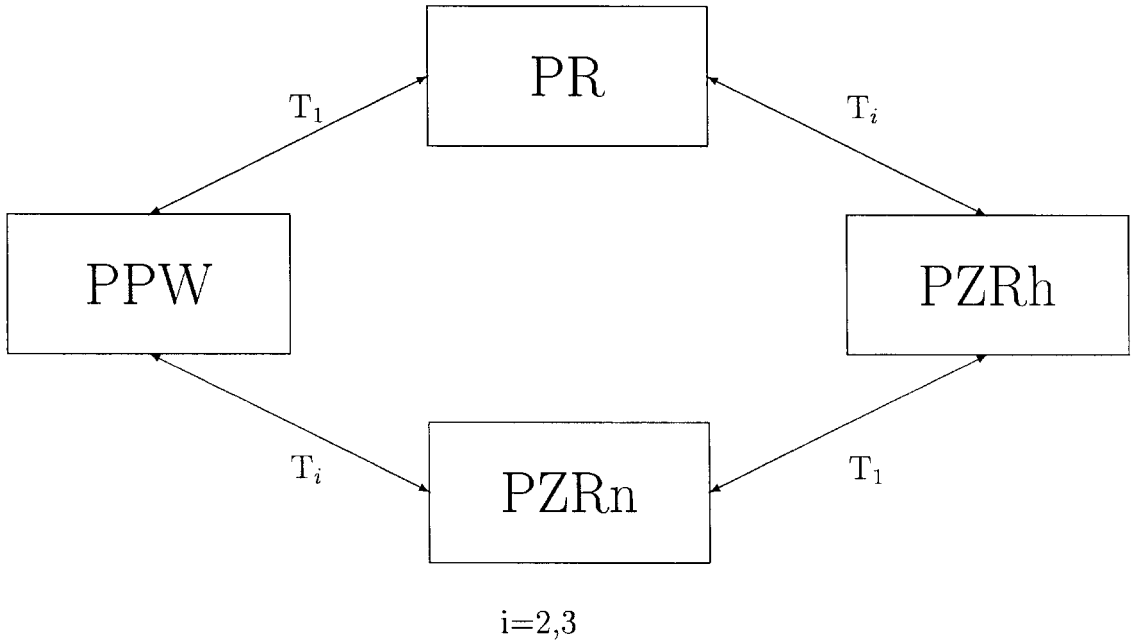


Figure 5. Block diagram of the transformation paths between planar radial (PR), planar pinwheel (PPW), and planar zigzag (PRZ) patterns. $T_1$ corresponds to the surface orientation change, $T_2$ corresponds to temperature change, and $T_3$ to fibre radius change.



the top row corresponds to the transformation $T_3$ between (PR) and (PZRh) patterns. Moving along the bottom row corresponds to the transformation $T_3$ between (PPW) and (PZRn) patterns.

4.1. *Solutions with symmetric boundary conditions*

With symmetric homeotropic boundary condition of $\phi(0)=\phi(1)=\pi/2$, the radial (PR) solution ($\phi=\pi/2$) exists for all $\mu$, as shown in the previous section. For $\mu>1$, $\mu=1$ and $1>\mu>\mu_c$, the trivial solution is the unique solution of the equation, where $\mu_c$ denotes a critical value of elastic anisotropy. The stability of the radial solution will be discussed later in this section.

Multiple oscillatory solutions, representing the homeotropic zigzag radial pattern (PZRh) are found when the ratio exceeds a certain value of $\mu_c$. For $\Delta u=1$, we found the critical value of $\mu_c=0{\cdot}092$.

Figure 8 shows a section of the bifurcation diagram, presented as the orientation amplitude ($\max|\phi|$) as a function of the elastic ansitropy of $\mu$. The horizontal (zero amplitude) line represents the radial (PR) solution and the five curves represent members of the PZRh family. The first bifurcation branch A represents an oscillatory solution with half-wavelength. The bifurcation occurs at $\mu=0{\cdot}092$, and the amplitude of the solution grows as $\mu$ decreases. At $\mu=0{\cdot}025$, the system bifurcates again and generates a new oscillatory solution branch B with one full wavelength. As $\mu$ decreases further, more branches are generated, representing solutions with one-half-wavelength C, two-wavelength, two-half-wavelength and so on. Figure 8 clearly shows the strong non-linear features of the model, with typical multiple bifurcations of the spatially constant solution (PR) into a family of spatially oscillatory solutions (PZRh) at critical values of elastic anisotropy ratio $\mu_{c,n}$ ($n=1, 2, \ldots$). For a given $\mu$, the number of the intersections of the amplitude curves with a vertical line gives the number of solutions, which for $\Delta u=1$ consists of PR and PZRh patterns. The figure also implies that $\mu_{c,n}-\mu_{c,n+1}$ is a monotonically decreasing function of $n$, and the $\lim_{n\to\infty}\mu_{c,n}=0$, indicating that the number of oscillatory solutions diverges as the elastic anisotropy vanishes. Another important feature of the figure is the amplitude ordering and amplitude growth with decreasing $\mu$. The amplitude of the shorter wave length mode is smaller than the bigger wave length mode. As typical of non-linear systems the amplitude growth is bounded.

Figure 9 shows the director orientation $\phi$ as a function of $u$, for $\mu=0{\cdot}01$, in which there are three solutions of PZRh (A, B, C) and one solution of PR (D). Figure 10 shows the eleven solutions for $\mu=0{\cdot}001$. As the figures show, by changing $\mu$ from 0·01 to 0·001, the number of the oscillatory solutions has increased from four to eleven. One can expect that as $\mu$ approaches zero, the number of branches will increase to infinity, meaning there will be infinite solutions to the equation. However, at any given finite value of $\mu$, there are only finite

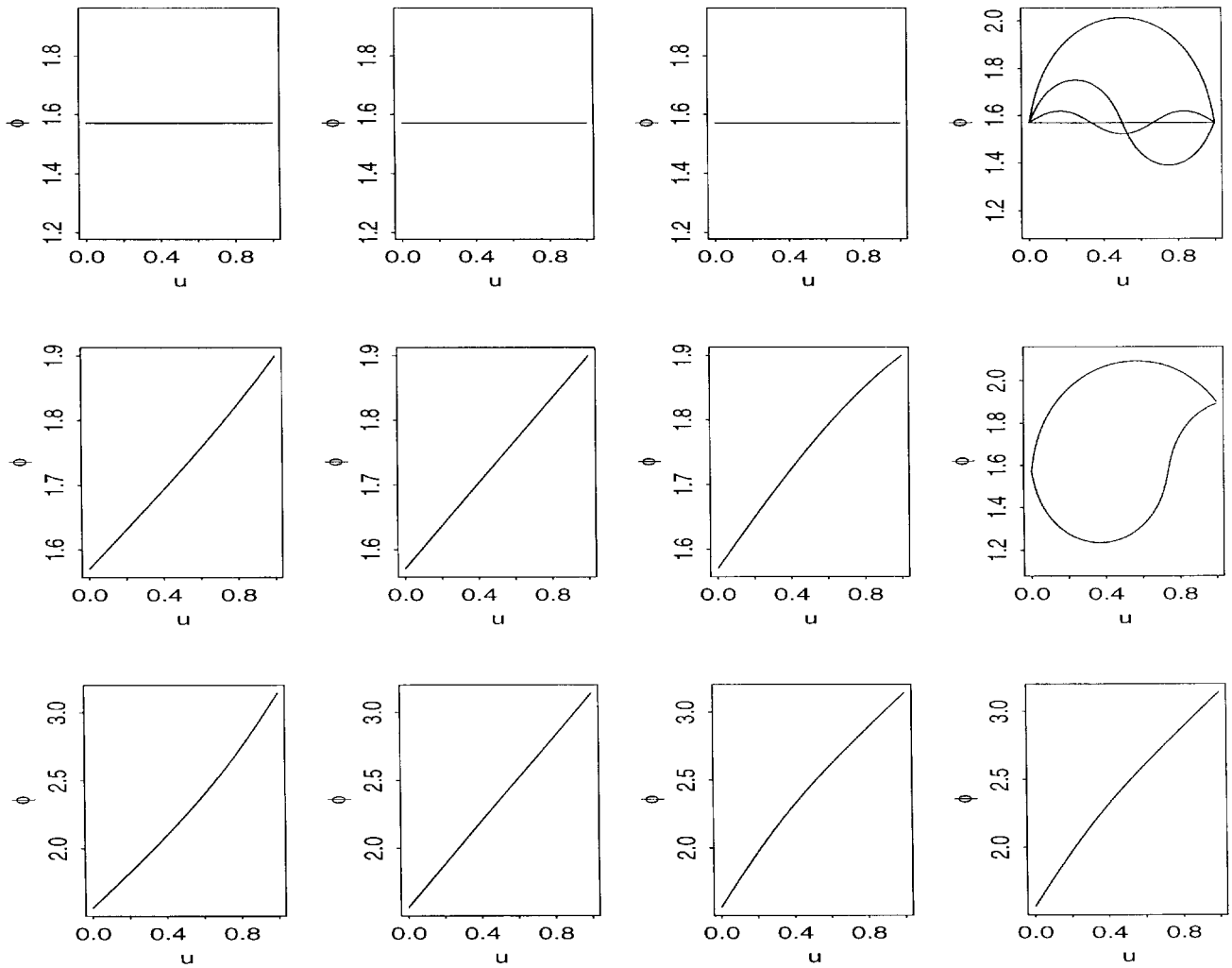


Figure 6. Summary of representative solutions to equation (9) for $\Delta u = 1$, and different parametric conditions. Symmetric boundary conditions (top row), asymmetric boundary conditions of ($\phi(1) = 1{\cdot}9$ (rad) (middle row) and asymmetric boundary conditions of $\phi(1) = \pi$ (bottom row). For elastic anisotropy, $\mu > 1$ (left column), $\mu = 1$ (left middle column), $1 > \mu > \mu_{c,1}$ (right middle column), and $\mu < \mu_{c,1}$ (right column).

number of solutions to the system. Note that figures 9 and 10 show that the solution with higher frequency has smaller amplitude than those with lower frequency, which is a very important feature of the system.

As described in the previous section, the solutions are found by solving the extended system of equations (12) and initial conditions (13). In order to find all the solutions to the system, we plot in figure 11 the functional dependence of $\phi(1) - \phi(0)$ on $\phi'(0)$, for $\mu = 0{\cdot}01$. The various horizontal lines correspond to various values of $\phi(1) - \phi(0)$. The line C represents the symmetric boundary conditions studied in this section (line A and B are discussed below), for which $\phi(1) = \phi(0) = \pi/2$. To find the number of solutions one can simply count the intersections of the horizontal lines with the curve. For line C, there are seven solutions: one trivial solution (PR), three oscillatory solutions (PRZh) with positive initial slope, and their three mirror images. (For brevity, we only show the oscillatory solutions with $\phi'(0) > 0$ in figure 9). It is clear from figure 11 that the above solutions are all the solutions of equation (9) for $\mu = 0{\cdot}01$ and symmetric boundary conditions.

To compare simulations with actual fibre textures (see, for example, figure 1 and [3, 4, 6]), it is useful to plot the molecular trajectories, i.e. the curves that are orthogonal to the local discotic director field. Similar to the streamline in fluid dynamics, the trajectory satisfies the geometrical relation: $\tan(\psi)(\mathrm{d}r/\mathrm{d}\theta) = r$, where $\psi = \phi - \pi/2$. To find the trajectory $\theta(r)$ we integrate the above differential equation using the previously computed director field $\phi(r)$. Here $\theta$ is the usual polar angle in cylindrical coordinates. Figure 12 shows the scientific

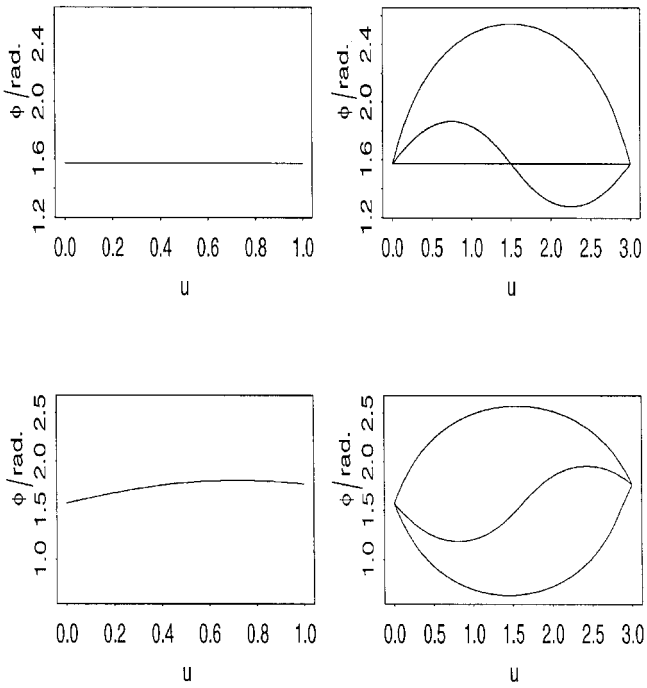


Figure 7. Summary of representative solutions to equation (9) for $\Delta u = 1$ (left column) and $\Delta u = 3$ (right column), for different outer boundary orientation, $\phi(u_o) = \pi/2$ (upper row) and $\phi(u_o) = 1{\cdot}77$ (rad) (lower row). Here $\mu = 0{\cdot}15$ is fixed for all cases.

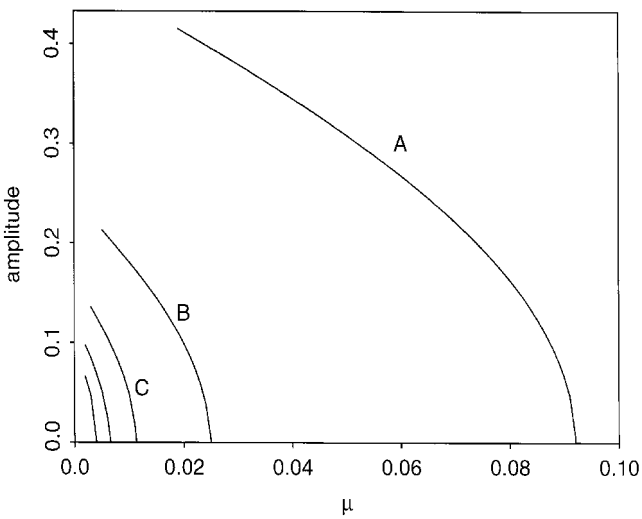


Figure 8. Bifurcation diagram. Amplitude of oscillatory solutions as a function of the elastic anisotropy $\mu$, for $\Delta u = 1$ and $\phi(1) = \pi/2$. It shows multiple solution branching and finite amplitude growth as $\mu$ decreases. The horizontal line corresponds to the ideal radial (PR) texture, while the bifurcation branches correspond to the oscillatory zigzag radial (PZRh) texture. For $\mu < 0{\cdot}092$ the PR solution is unstable. For $\mu < 0{\cdot}028$ there are multiple oscillatory solutions.

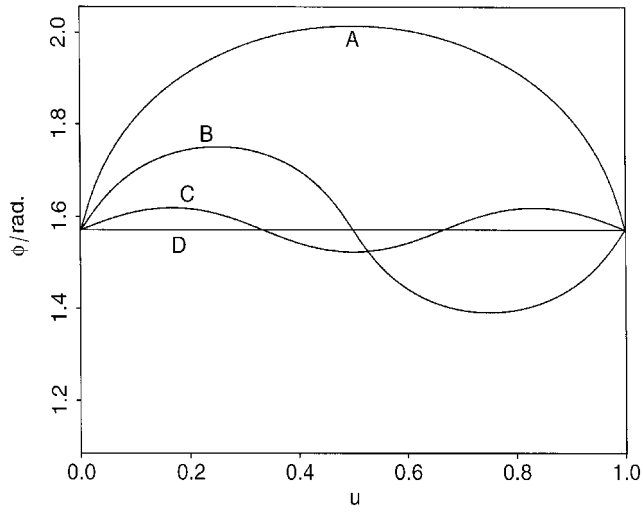


Figure 9. Director orientation $\phi$ (rad) as a function of dimensionless distance $u$, for $\Delta u = 1$, $\mu = 0{\cdot}01$ and $\phi(1) = \pi/2$. Curve D denotes the PR solutions while curves A, B, and C are members of PZRh family. The four solutions correspond to the four intersections of the horizontal line C with the curve in figure 11, for $\phi'(0) \geqslant 0$. The three mirror image oscillatory solutions are now shown.

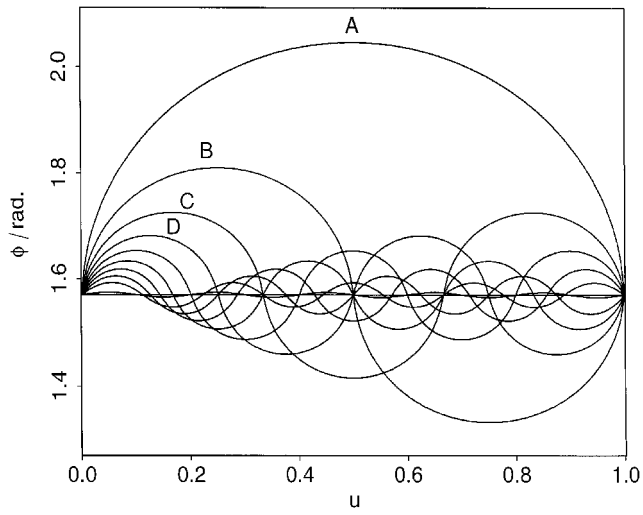


Figure 10. Director orientation $\phi$ (rad) as a function of dimensionless distance $u$, for $\Delta u = 1$, $\mu = 0{\cdot}001$ and $\phi(1) = \pi/2$. For this relatively small value of $\mu$ there are ten oscillatory solutions (PZRh) and the radial (PR) solution. Again, the mirror image oscillatory solutions are not shown for clarity. Note the significant increase in the number of solutions as $\mu$ changes from 0·01 (see figure 9) to 0·001.

visualizations of the curves A, B, C and D in figure 10. The presence of spatial oscillations are clearly seen. In visualization A it is seen that the disk start with zero angle, indicating that the director angle is $\pi/2$. The trajectory shows an increase and then decrease of the director angle, ending at the outer boundary with the same

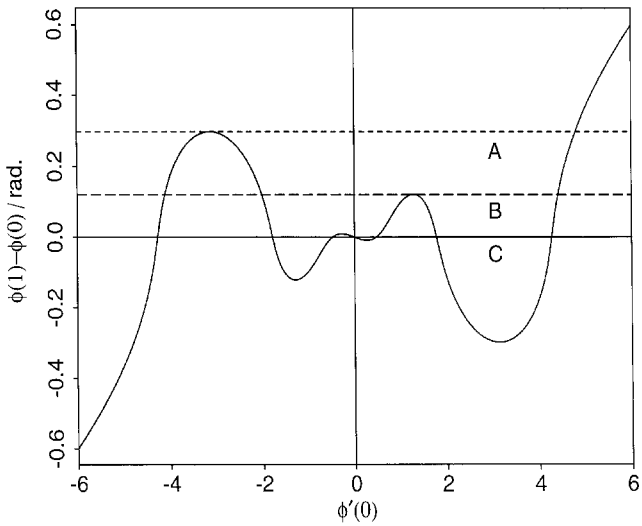


Figure 11. Functional relation of the outer boundary orientation $\phi(u_o)$ and the initial slope $\phi'(0)$, for $\Delta u = 1$ and $\mu = 0{\cdot}01$. $\phi(1) - \phi(0)$: 0 (full line C); 0·120 (long dashed line B); 0·298 (short dashed line A). Solutions to any value of outer boundary orientation can be found by drawing a horizontal line at the give value of $\phi(u_o)$, the initial slope of the soutions are given by the intersection of the line and the curve.



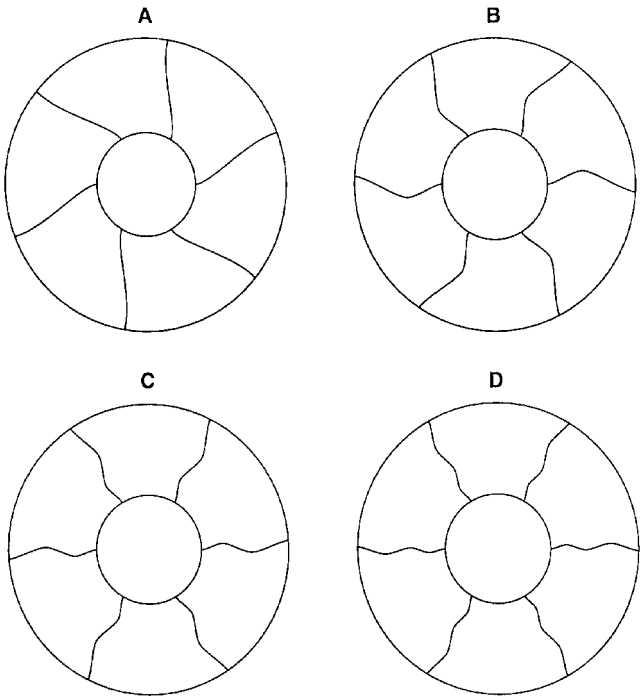


Figure 12. Scientific visualizations of disk trajectories for the oscillating zigzag (PRZh) solutions A, B, C, and D, shown in figure 10. The trajectories represent lines (of constant orientation) parallel to the molecular disks. Multiple oscillations are visible in B, C, and D.

angle as $\phi(0)$. In visualization B, corresponding to the solution with one full wavelength in figure 10, the oscillation is more visible. In visualizations C and D, there are more oscillations but with smaller amplitude.

Next we discuss the solution branching and texture behaviour of the PZRh pattern, for $\Delta u = 2$. Since $u(r_c) = 1$, this increment of $\Delta u$ corresponds to a larger outer radius. Figure 13 shows the director orientation as a function of $u$, for $\mu = 0{\cdot}005$, corresponding to four members of the PZRh family. The figure shows that the main features of the oscillatory solutions remain invariant. For this parametric value we show four periodic solutions, again with higher amplitude corresponding to longer wavelength. Comparing the solution A in figure 13 to solution C in figure 10, it is seen that increasing $\Delta u$ results in amplitude growth. Again, to compare the theoretical results to actually patterns, we use visualizations, computed as described above. We note that in the visualization we have, without loss of information, kept the outer radius fixed. Figure 14 shows four visualizations (A, B, C, D) of members of the PZRh family, corresponding to the director profiles shown in figure 13. The multiple solutions suggest multiple configurations for the same set of elastic constants $K_1$ and $K_3$, which in reality would mean abundant oscillatory patterns. In these disk trajectories, we can see the finite amplitude oscillation that certainly captures the basic features of the cross-section of a mesophase carbon fibre displaying a radial zigzag texture (see figures 1 and 7 of [6]).

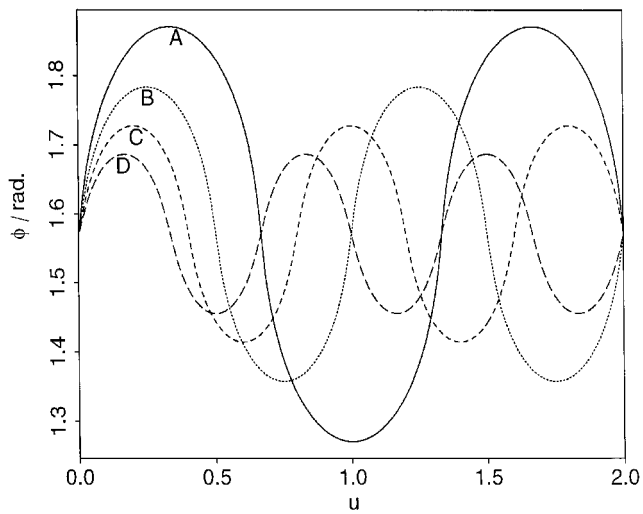


Figure 13. Director orientation $\phi$ (rad) as a function of dimensionless distance $\mu$, for $\Delta u = 2$, $\mu = 0{\cdot}005$, and $\phi(2) = \pi/2$. The four oscillatory zigzag radial solutions are members of the PZRh family, and are locally stable solutions to equation (9). Note the increase in amplitude for solutions with the same wave number but with $\Delta u = 1$ (see figure 10).

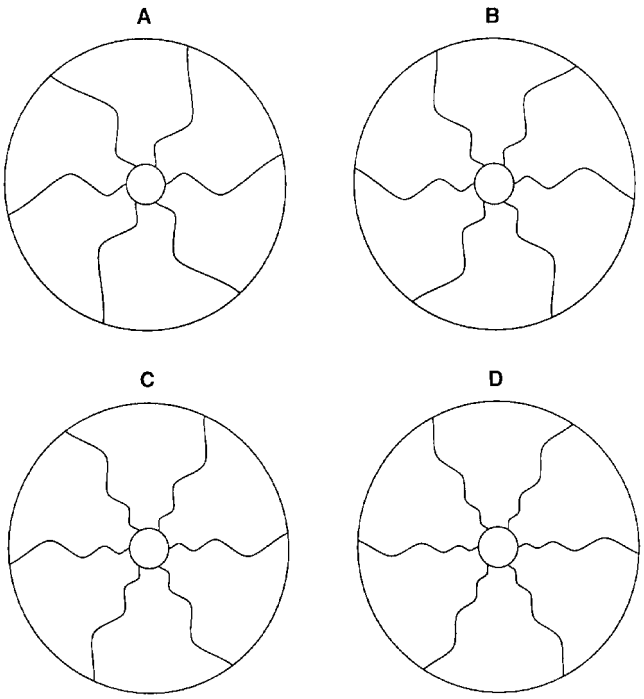


Figure 14. Four scientific visualizations of members of PZRh family of oscillatory zigzag radial solutions shown in figure 13. Note the finite amplitude oscillations, as in industrial mesophase carbon fibres [6].



To establish the actual observability of the predicted spatially oscillatory radial zigzag patterns, we have to determine the stability properties of the numerical solutions to equation (9). The most efficient way to examine the stability of the solutions obtained is to compute the second variation of the free energy integral [20]. By setting $\phi(u) = \phi^*(u) + \delta\phi(u)$ and expanding the free energy $F$ in power series of $\delta\phi(u)$ up to the second order, we get

$$\Delta F = \int [f(\phi^* + \delta\phi, \phi^{*\prime} + \delta\phi') - f(\phi^*, \phi^{*\prime})]\,\mathrm{d}\mu$$
$$= (\delta F)_1 + (\delta F)_2 + \cdots \tag{14}$$

where

$$(\delta F)_1 = \int \left[\frac{\partial f}{\partial \phi} - \frac{\mathrm{d}}{\mathrm{d}u}\frac{\partial f}{\partial \phi'}\right]_{\phi=\phi^*} \mathrm{d}u, \tag{15}$$

and

$$(\delta F)_2 = \int \left[\frac{\partial^2 \mathrm{f}}{\partial \phi^2}(\delta\phi)^2 + 2\frac{\partial^2 f}{\partial \phi\,\partial \phi'}\delta\phi\delta\phi' + \frac{\partial^2 f}{\partial \phi^2}(\delta\phi')\right]_{\phi=\phi^*} \mathrm{d}u \tag{16}$$

where $(\delta F)_1$ is the first variation of the free energy, and $(\delta F)_2$ is the second variation. By letting $(\delta F)_1 = 0$, we find the extremum free energy configuration $\phi^*$. Therefore, the sign of the increment $\Delta F$ coincides with the sign of $(\delta F)_2$. Replacing $f$ from equation (8), we obtain the following integral:

$$(\delta F)_2 = \int \{[K_3 - K_1] \times (\cos 2\phi - 2\phi' \sin 2\phi - \phi'^2 \cos 2\phi)(\delta\phi)^2 + [K_3 - K_1](2\cos 2\phi - 2\phi' \sin 2\phi)\delta\phi\delta\phi' + (K_1 \sin^2\phi + K_3 \cos^2\phi)(\delta\phi')^2\}\,\mathrm{d}u. \tag{17}$$

Evaluating the integral for each of the numerical solutions, we compute the second variation of the free energy and thus are able to determine the free energy increment induced by an arbitrary small perturbation. Figure 15 shows the second variation $(\delta F)_2$ as a function of the amplitude of an oscillatory solution belong to the PZRh patterns. The parametric conditions are $\mu = 0{\cdot}001$ and $\Delta u = 1$. The dots in figure 15 are second variations of the oscillatory solutions whose director profiles are shown in figure 10. The figure shows that the second variation is always positive. Therefore, based on the argument above, all the oscillatory solutions are locally stable to small perturbations. We may conclude that the oscillatory trajectories are the stable configurations for this type of boundary condition, thus proving abundant multistability. As in other non-linear systems that exhibit multistability, a specific member of the PZRh family will be selected if the initial conditions are included in the

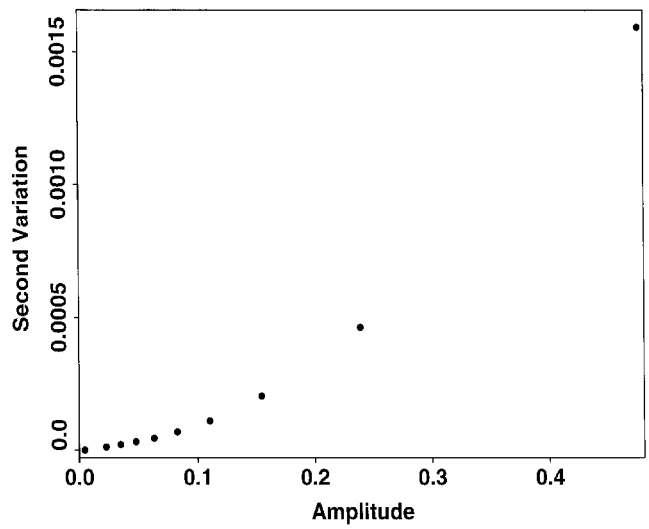


Figure 15. Second variation $\delta F_2$ of the free energy as a function of the amplitude for the oscillatory zigzag (PZRh) solutions shown in figure 10. Since $\delta F_2 > 0$ the oscillatory zigzag solutions are all locally stable, thus proving the presence of multistability phenomena.

domain of attraction of that particular solution. Since the domain of attractions of the various solutions are function of $(\mu, \Delta u, \phi(u_o) - \phi(0))$, a particular initial texture may evolve to different members of the PZR family, according to the governing parameter values.

The second variation method is successful in establishing the stability of the oscillatory solutions, however, it fails for the trivial solution. In the integral (16), one can see that substituting the trivial solution gives $\phi^* =$ constant, $\delta\phi = 0$, and $\delta\phi' = 0$, and thus the integral will be zero. In fact, for the trivial solution any variation will be identically zero. Therefore we cannot determine the stability of trivial solution under any given parametric conditions using this method and have to use another analytical method. Consider a small perturbation on the constant solution [10],

$$\phi(u) = \frac{\pi}{2} + \delta(u), \tag{18}$$

where $\delta(u)$ is a small perturbation which satisfies

$$\delta(0) = \delta(1) = 0. \tag{19}$$

Substitute (18) into equation (8) and expand the result, then the energy density difference to second order is given by

$$f_2 = \frac{K_1}{2}(\delta^2 + 2\delta'\delta + \delta'^2) + \frac{K_3}{2}(-\delta^2 - 2\delta\delta') \tag{20}$$

Applying the above expression in the free energy integral, using interpretation by parts, and taking into account the boundary condition of $\delta(u)$, the difference of the total free energy will be

$$\begin{aligned}\Delta F &= \int f_2 \, \mathrm{d}u \\ &= \frac{1}{2}\int \{K_1(\delta^2 + 2\delta\delta' + \delta'^2) + K_3(-\delta^2 - 2\delta\delta')\} \, \mathrm{d}u \\ &= \frac{1}{2}\int \{(K_1 - K_3)\delta - K_1\delta''\} d \, \mathrm{d}u. \end{aligned} \tag{21}$$

If the above integral is positive, then the configuration is stable to small perturbations. If the integral is positive, it means any small perturbation will increase the total free energy, thus the constant solution would be a local minimum of the free energy and therefore is stable to any perturbation. To determine if the integral is positive, we therefore consider the following eigenvalue problem:

$$\frac{K_1 - K_3}{2}\delta - \frac{K_1}{2}\delta'' = \lambda\delta, \tag{22}$$

with the boundary conditions of $\delta(0) = \delta(1) = 0$. When the above eigenvalue problem has positive eigenvalues, that is $\lambda > 0$, then the free energy integral becomes

$$\Delta F = \frac{1}{2}\int \{(K_1 - K_3)\delta - K_1\delta''\}\delta \, \mathrm{d}u = \int \lambda\delta^2 \, \mathrm{d}u \tag{23}$$

which is positive definite, and we can then determine the stability of the configuration based on the previous argument. Solving the eigenvalue equation, we obtain

$$\lambda = \frac{1}{2}\left\{K_1 - K_3 + 1\left(\frac{n\pi}{\Delta u}\right)^2\right\}; \qquad (n = 1, 2, 3, \ldots). \tag{24}$$

It follows that if $\lambda < 0$, the pure bend (radial) structure will be unstable to any small perturbation. We find the stability threshold of the radial texture is

$$\mu < \mu_{c,n} = \frac{1}{1 + \left(\frac{n\pi}{\Delta u}\right)^2}; \qquad (n = 1, 2, 3, \ldots) \tag{25}$$

Putting $\Delta u = 1$ and $n = 1$ in the above inequality, we find $\mu_{c,1} = 0{\cdot}092$, which is equal to the value of $\mu$ corresponding to the bifurcation point found numerically, reported above in this section. A comparison of analytical values and the numerical values of $\mu_{c,n}$ is shown in table 1. The excellent agreement validates the correctness of the numerical results.

According to the general theory of eigenvalue problems, the eigenvalues obtained for equation (22) present the values of $\lambda_n$ at which non-trivial solutions can be found. The existence of non-trivial solutions for these values of $\lambda_n$, which corresponds to the values of $\mu_{c,n}$, arise from the bifurcations of the constant solution branch at these points. The exact correspondence between the eigenvalues and the bifurcations is the reason behind the consistency between analytical and numerical results, as shown in table 1. In addition, the small amplitude oscillatory solutions can be closely approximated by the corresponding eigenfunctions derived above. A discussion giving the mathematical details of the eigenvalue problem is given in the Appendix.

According to the inequality (25), the value of $\mu_{c,1}$

Table 1. Elastic anisotropy ($\mu$) thresholds for birth of oscillatory modes.

| $\mu_{c,n}$ | Theoretical value | Numerical value |
|---|---|---|
| $n = 1$ | 0·09199 | 0·09200 |
| $n = 2$ | 0·02470 | 0·02500 |
| $n = 3$ | 0·01113 | 0·01127 |
| $n = 4$ | 0·006293 | 0·006265 |
| $n = 5$ | 0·004036 | 0·003999 |

depends on $\Delta u$. For all $\Delta u$, $\mu_{c,1}$ is always a positive number and $\mu_{c,1} \leqslant k$, where $k < 1$. This means the bifurcation will not occur as soon as $K_1 < K_3$, instead, the trivial solution will be stable until the ratio $K_1/K_3$ exceeds a certain threshold $\mu_{c,1}$. As $\Delta u$ increases, $\mu_{c,1}$ increases accordingly. So, for $\Delta u > 1$, the critical value of $\mu_{c,1}$ can be very close to 1. Therefore for relatively large fibres, a small elastic anisotropy of the type studied here ($\mu < 1$, that is, the bend constant larger than the splay constant) will induce a bifurcation in the equation (9), corresponding to a transformation between the radial texture and the zigzag radial texture. This is a reason for the frequent observation of oscillatory zigzag textures in actual mesophase fibres [6].

Although this paper is restricted to patterns that arise from continuous transformations of the ideal pure bend planar radial pattern, here we briefly discuss a significant fact regarding the stability of the onion patterns in the presence of $\mu < 1$ (see figure 1) since this has direct relevance to our objectives. In contrast to the frequently observed zigzagging in radial patterns, oscillations and zigzagging of the onion patterns have apparently not been reported. It is thus important to explain this absence, and at the same time establish that our criteria that lead to the frequently observed PRZh patterns would not lead to zigzagging in the onion texture, thus adding validity to our analysis. The onion pattern is found for symmetric boundary conditions: $\phi(0) = \phi(1) = 0$. The trivial soluton for this type of boundary condition is $\phi = 0$. This type of configuration represents a pure splay mode, that is, the concentric texture. To determine its stability, we follow the same method elaborated above, and add a small perturbation $\delta(u)$ to the trivial solution,

$$\phi = \delta(u) \tag{26}$$

with boundary condition of $\delta(0) = \delta(1) = 0$. Then to second order, the perturbed energy is given by

$$f_2 = \frac{K_1}{2}(-\delta^2 - 2\delta'\delta) + \frac{K_3}{2}(\delta^2 + 2\delta'\delta + \delta'^2). \tag{27}$$

Thus we obtain

$$\Delta F = \int f_2 \, \mathrm{d}u = \frac{1}{2}\int \{(K_3 - K_1)\delta - K_3\delta''\}\delta \, \mathrm{d}u. \tag{28}$$

Similarly, we consider the eigenvalue problem of

$$\frac{K_3 - K_1}{2}\delta - \frac{K_3}{2}\delta'' = \lambda\delta, \tag{29}$$

with boundary condition of $\delta(0) = \times \delta(1) = 0$. The eigenvalues now are given by

$$\lambda = \frac{1}{2}\left\{K_3 - K_1 + K_3\left(\frac{n\pi}{\Delta u}\right)^2\right\}, \qquad (n = 1, 2, 3, \ldots). \tag{30}$$

It follows that, if $K_1 < K_3$, when the radial oscillatory patterns are often observed, the eigenvalues in (30) will always be positive, and the onion pattern will be stable to any small perturbations. Therefore, there is no oscillatory solution to the equilibrium equation under this type of boundary and elastic anisotropy conditions. Hence there will be no oscillations to the pure splay mode, any perturbations to this pattern will decay to zero, and a zigzag onion pattern would never occur, which is in agreement with the facts.

### 4.2. *Solutions with asymmetric boundary conditions*

In this section we analyse the new features arising from non-symmetric boundary conditions $\phi(0) = \pi/2$, $\phi(1) = \alpha$, with $\pi/2 < \alpha < \pi$. The first important feature is that the PR pattern does not exist, and its role is taken up by the planar pinwheel pattern PPW. Instabilities deduced by elastic anisotropies lead to bifurcations involving PPW and PZRn branches, here PZRn stands for planar non-homeotropic zigzag radial pattern (see figure 4).

As shown in the second row of figure 6, for $\phi(1) = 1{\cdot}869$, the solution for $\mu > 1$ is unique and monotonic. For $\mu = 1$, the solution is linear. We can derive this linear solution analytically. By setting $K_1 = K_3$ in the equilibrium equation, we find

$$K_1\phi'' = 0 \tag{31}$$

and the equation has a unique linear solution for $K_1 = K_3$.

For $\mu < 1$, similar to the situation with symmetric boundary conditions, the bifurcation will not occur until $\mu$ exceeds the critical value of $\mu_{c,1}$, but now $\mu_{c,1}$ will be a function of $\phi(u_o)$ as well as of $\Delta u$. Figure 16 shows the computed bifurcation diagram in the $(\mu, \phi(u_o))$ plane. The full line denotes the bifurcation for $\Delta u = 1$; for symmetric boundary condition, i.e. $\phi(1) = \phi(0) = \pi/2$, the bifurcation occurs at $\mu_{c,1} = 0{\cdot}092$. As $\phi(1)$ increases, the critical value of bifurcation $\mu_{c,1}$ decreases. Above the full line, equation (9) has a unique locally stable monotonic solution (PPW), and below the full line the equation has multiple locally stable solutions (PZRn). The dashed line denotes the bifurcation between PPW and PZRn, for $\Delta u = 2$. Note the significant increase of $\mu_c$ as $\Delta u$ increases. For $\Delta u = 2$ with symmetric boundary conditions, the bifurcation occurs at $\mu = 0{\cdot}285$. When substituting $\Delta u = 2$ into the inequality (25), we obtain $\mu_c = 0{\cdot}288$, which agrees with the numerical results. Again above the dashed line the locally stable solutions are

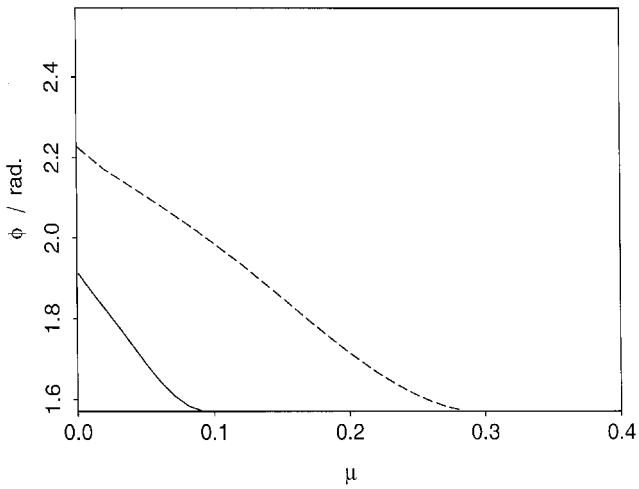


Figure 16. Bifurcation diagram in the elastic anisotropy $\mu$ outer boundary condition plane. Fibre size $\Delta u = 1$ (full line), 2 (dashed line). The full (dashed) line divides the parametric plane into two solution regions. The one above the line is where equation (9) has a unique solution, and the one below the line as well as the line itself is where the equation has multiple oscillatory solutions.

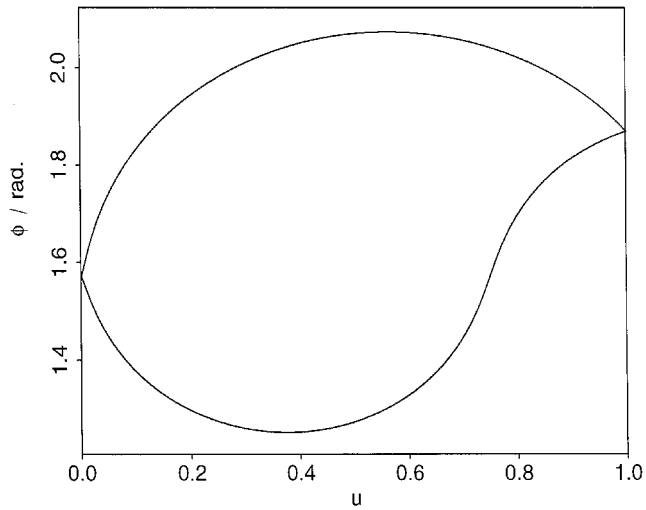


Figure 17. Director orientation $\phi$ (rad) as a function of $u$, for $\Delta u = 1$, $\mu = 0{\cdot}01$ and $\phi(1) = 1{\cdot}868$. The two solutions are members of the PZRn family. They correspond to the two intersections of line A with the curve in figure 11.



PPW solutions, while below the dashed line there are multiple locally stable PZRn solutions.

For $\mu_{c,1} < \mu < 1$, the equation has a unique non-linear monotonic solution, representing the PPW pattern. The difference between solutions for $\mu < 1$ and solutions for $\mu > 1$ is their concavity, as shown in the panels of the middle row of figure 6. The change of concavity is due to the change of elastic constants which make splay deformation more favourable for $K_1 < K_3$, and bend deformation favourable for $K_1 > K_3$. Below the dashed line, when $\mu < \mu_{c,1}$, the system will have multiple solutions. The functional relation of $\phi'(0)$ and $\phi(1)$ shown in figure 11 can also be used to find the solutions for asymmetric boundary conditions; line A corresponds to $\phi(1) = 1{\cdot}868761$, and line B to $\phi(1) = 1{\cdot}692094$. As shown in figure 11, there are two solutions for $\phi(1) = 1{\cdot}868761$, and four solutions for $\phi(1) = 1{\cdot}692094$. Figure 17 shows the director orientation $\phi$ as a function of $u$, for $\phi(1) = 1{\cdot}868761$ and $\mu = 0{\cdot}01$, corresponding to the solutions found from line A in figure 11. The two solutions are members of the PZRn family, with the upper curve representing the first mode and the lower curve the second mode. Figure 18 shows the director orientation $\phi$ as a function of $u$, for $\phi(1) = 1{\cdot}692094$ and $\mu = 0{\cdot}01$, corresponding to the solutions found from line B in figure 11. The four solutions are members of the PZRn family. Following the visualization methodology presented above, figure 19 shows the disk trajectories for the four solutions (A, B, C, D) shown in figure 18. Since solutions A and D in figure 18 display incomplete oscillations, the corresponding disk trajectories also display

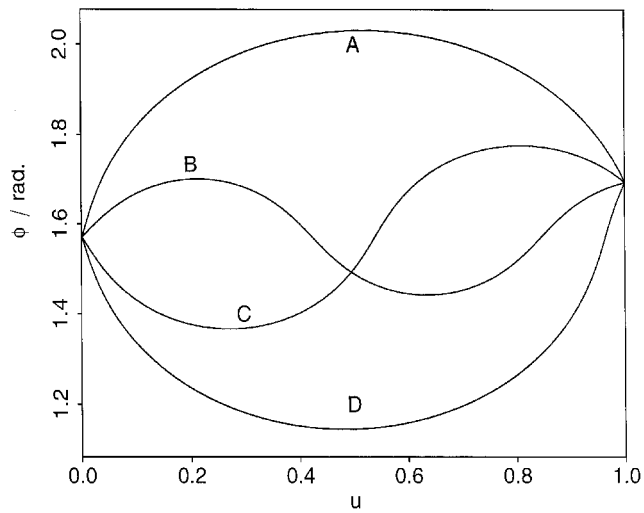


Figure 18. Director orientation $\phi$ (rad) as a function of $u$, for $\Delta u = 1$, $\mu = 0{\cdot}01$ and $\phi(1) = 1{\cdot}692$. The four solutions are members of the PZRn family. They correspond to the four intersections of line B with the curve in figure 11.

incomplete oscillation. For solution B and C in figure 18, the oscillations in the disk trajectories are clearer.

Again here we wish to explore the role of fibre size on the main features of the bifurcation and multistability by plotting the trajectories of PPW and PZRn patterns. Figure 20 shows four solutions for $\Delta u = 2$, $\mu = 0{\cdot}005$, and $\phi(2) = 1{\cdot}8$ (rad), which belong to the PZRn family. The corresponding visualization of disk trajectories are shown in figure 21. Here, as in the previous section, an increase in $\Delta u$ brings an increase in the amplitude in the oscillations. For the disk trajectories representing

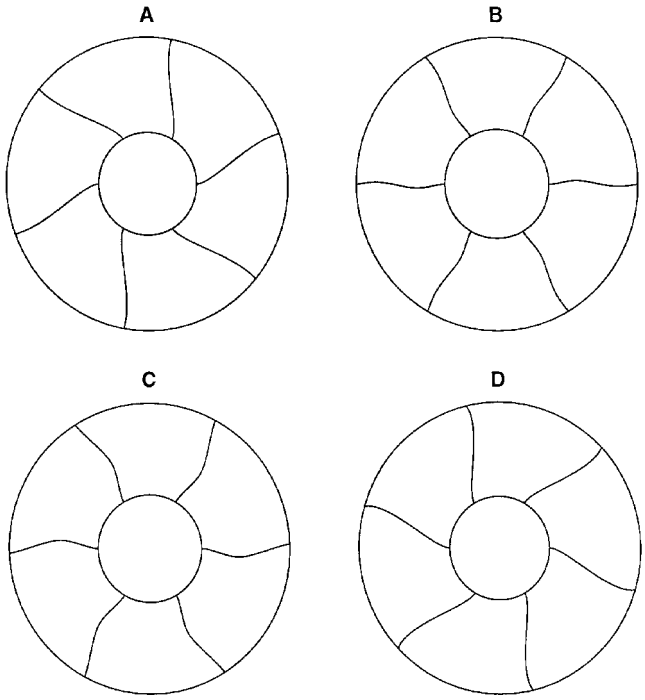


Figure 19. Scientific visualizations of disk trajectories for the oscillatory zigzag (PZRn) solutions A, B, C, and D, shown in figure 18. Finite amplitude oscillations are visible in B and C. The different spiral directions in A and D are due to the different values of $\phi'(0)$ for solutions A and D in figure 18.

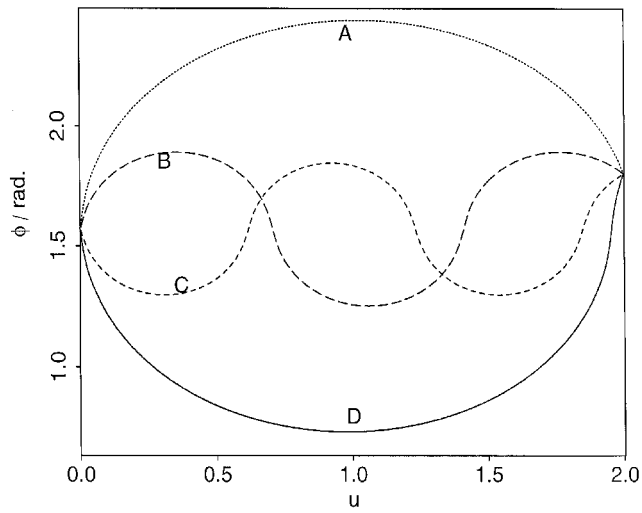


Figure 20. Director orientation $\phi$ (rad) as a function of $u$, for $\Delta u = 2$, $\mu = 0{\cdot}005$ and $\phi(2) = \pi/2$. The solutions are members of the PZRn family. Note the amplitude increase for these solutions in comparison to the PZRn solutions with the same wave numbers but smaller $\Delta u$ ($\Delta u = 1$) shown in figure 18.

solution B and C in figure 20, one can clearly see the oscillations to avoid free energy costs.

In the following we explore the main differences that

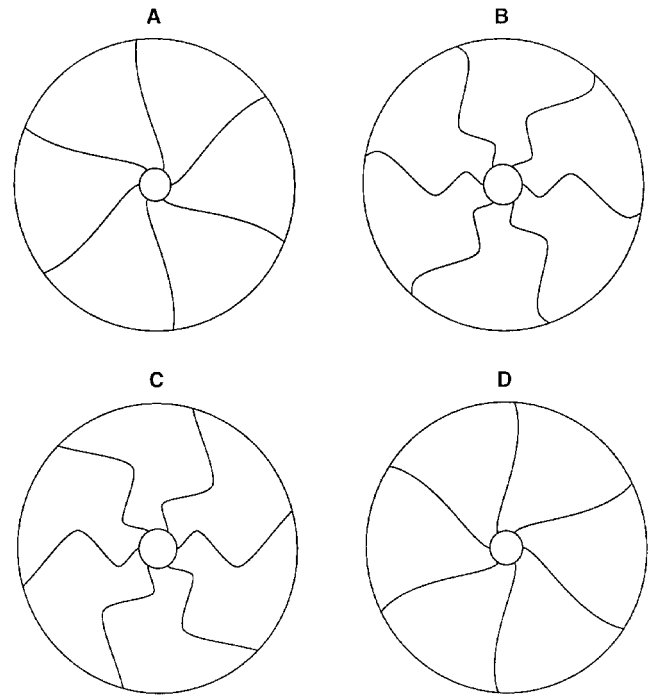


Figure 21. Scientific visualizations of disk trajectories for the oscillatory zigzag (PZRn) solutions A, B, C, and D, shown in figure 20.

arise in the solution behaviour and multistability phenomena, in the presence of symmetric and asymmetric boundary conditions. Figure 11 shows that the solutions are not symmetric as in the case of symmetric boundary conditions. For solutions with $\phi(1) = 1{\cdot}692094$, the mirror configurations are the solutions at $\phi(1)_{\text{mirror}} = \pi - \phi(1)$. Another feature that is different from the case with symmetric boundary condition, is that as $\mu$ decrease further, the number of solutions will increase to a certain finite value, which depends on the value of boundary orientation at the outer cylinder, as opposed to the monotonic increase in the number of solutions (PZRh) for symmetric boundary conditions. The reason is that for oscillatory PZRn and PZRh solutions, the solution amplitude has to be larger than $\phi(u_o) - \phi(0)$. However, since a solution with higher frequency has smaller amplitude, and the lowest possible amplitude would be $\phi(u_o) - \phi(0)$, therefore even if $\mu$ continues to decrease, there will be no new solutions and the number of solutions with amplitude larger than $\phi(u_o) - \phi(0)$ will therefore always be finite.

### 4.3. *Solutions for asymmetric boundary conditions with large asymmetry*

In this section we briefly explore the new phenomena that arise due to large asymmetry in the boundary conditions, and report on the representative case of $\phi(u_o) = \pi$. For the case with boundary condition of

$\phi(0)=\pi/2$, $\phi(1)=\pi$, we find only one solution for all different values of $\mu$, as shown in the third row of figure 6. Again, the concavity of the solution will change as $\mu$ changes from $\mu>1$ to $\mu<1$. As $\mu$ diverges ($\mu\to\infty$) the solution is boundary-layer like, with the boundary layer located next to $u=1$. While when $\mu$ vanishes ($\mu\to 0$) the boundary layer is located next to $u=0$. Figure 22 shows the director orientation $\phi$ as a function of $u$, for three different values of $\mu$: 1000 (dashed), 1 (dotted), and 0·001 (full). The linear solution is obtained for $K_1=K_3$ ($\mu=1$), and the concavity of the other two curves is in agreement with the expected boundary layer mode that minimizes the free energy.

For this type of boundary condition, there are no bifurcations in the equilibrium equation (9). As shown above, the amplitude of any oscillatory solution has to be larger or equal to $\phi(u_o)-\phi(u_o)$, which in the present case is $\pi/2$. However, since the increase of frequency of any solution will result in a decrease in amplitude and the existing monotonic solution has an amplitude of $\pi/2$, any oscillatory solution would have to have an amplitude less than $\pi/2$, yet it has to have a maximum of $\phi(u_o)=\pi$ in order to satisfy the boundary condition at the outer cylinder. The contradiction makes the existence of oscillatory solutions impossible. Therefore we can conclude that for this type of boundary conditions, there exists no oscillatory solutions to equation (9) at any value of $\mu$.

In this section we have presented numerical results for three types of boundary conditions. A summary of the results is shown in table 2. In general, for the symmetric type of boundary conditions of $\phi(u_c)=\phi(u_o)=\pi/2$, equation (9) has a unique constant solution for $\mu>\mu_{c,1}$. When $\mu<\mu_{c,1}$, the constant solution becomes unstable to small perturbations, the system undergoes a bifurcation and generates a family of branches of oscillatory solutions (PRZh). For the symmetric boundary condition of $\phi(u_c)=\phi(u_o)=0$, we have shown that while $\mu<1$ there is only constant solution to the equation. For asymmetric boundary conditions with $\phi(u_c)=\pi/2$ and $\phi(u_o)<\pi$, the equation has a unique monotonic solution (PPW) for $\mu>\mu_c$. Particularly, at $K_1=K_3$, the equation has a unique linear solution. As $\mu<\mu_c$, the stem will bifurcate and generate branches of oscillatory solutions (PZRn). For the symmetric boundary condition of $\phi(u_o)=\pi$, there is a unique monotonic solution (PPW) to the equation for all value of $\mu$.

Table 2. Summary of parametric ranges and stability properties of orientation textures.

| Boundary condition $\phi(0)=\pi/2$ | $\mu=K_1/K_3$ | Solution type | Figures |
|---|---|---|---|
| $\phi(u_o)=\pi/2$ | $\mu>1$ | PR stable | 6 |
| | $\mu=1$ | PR stable | 6 |
| | $\mu_c<\mu<1$ | PR stable | 6 |
| | $\mu<\mu_c$ | PZRh stable | 9, 10, 14 |
| $\pi/2<\phi(u_o)<\pi$ | $\mu>1$ | PPW concaving up, stable | 6 |
| | $\mu=1$ | PPW stable | 6 |
| | $\mu_c<\mu<1$ | PPW concaving down, stable | 6 |
| | $\mu<\mu_c$ | PZRh stable | 17, 18, 20 |
| $\phi(u_o)=\pi$ | $\mu>1$ | PPW concaving up, stable | 22 |
| | $\mu=1$ | PPW stable | 22 |
| | $\mu<1$ | PPW concaving down, stable | 22 |

PR: planar radial pattern, PZRh: homeotropic planar zigzag radial pattern, PZRn: non-homeotropic planar zigzag radial pattern, PPW: planar pinwheel pattern.

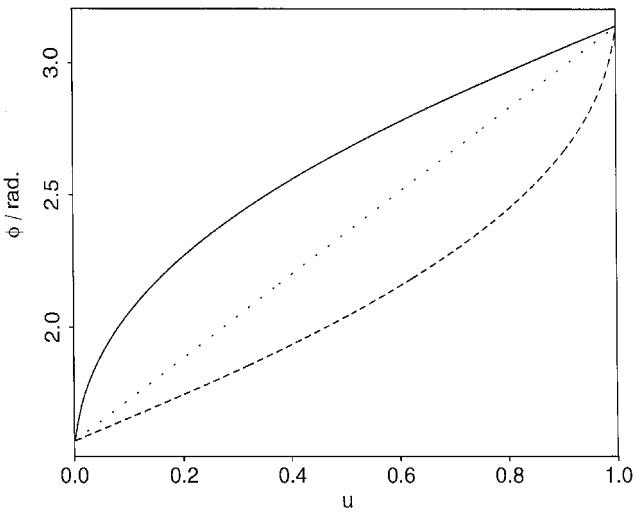


Figure 22. Director orientation $\phi$ (rad) as a function of $u$, for $\Delta u=1$ and $\phi(1)=\pi$, for $\mu$: 0·001 (full line); 1 (dotted line); 1000 (dashed line). For $\mu_1=1$ ($K_1=K_3$) the solution is linear, for $\mu_1\ll 1$ ($K_1\ll K_3$) the solution is concave down, and for $\mu_1\gg 1$ ($K_1\gg K_3$) concave up, as dictated by energy minimization.

## 5. Conclusions

In summary, we have presented a detailed numerical analysis to a model that is sufficiently accurate to provide plausible explanation to the pattern formation process that arises during the industrial melt fibre spinning of carbonaceous mesophases, using discotic nematic liquid

crystal precursors. In addition, a comprehensive analysis of pattern formation in discotic nematics confined to an annular geometry has been presented. Analysis on the flow leads to the conclusion that the net effect of the extensional flow in the fibre spinning process on the texture formation is to keep the director in the $\psi - r$ transverse plane. Therefore, given sufficient long process times as compared to reorientation times, the transverse radial zigzag pattern is selected by the minimization of the splay–bend elastic free energy per unit fibre length. Numerical studies of the solution types to the equilibrium equation (9) derived from Frank's elastic energy model indicate that the equilibrium equation displays a wide variety of solution types in the parametric space spanned by the elastic anisotropy, the fibre diameter, and the boundary conditions. The basic planar patterns with singular cores are the radial pattern, the pinwheel pattern, and the zigzag radial pattern. Only the zigzag radial pattern exhibits multistability. Multistability of oscillatory solutions displaying the radial zigzag patterns are found for: larger elastic anisotropy ($K_3 > K_1$), weaker boundary condition asymmetries, and larger fibres.

Numerical as well as analytical results show that the occurrence of oscillations in radial patterns is due to the elastic splay–bend anisotropy. This is because the energy minimization process of the free energy would select the most cost-effective pattern to lower the total free energy. Therefore, as the bend configuration becomes costly, the system will naturally select splay deformation over the bend deformations. Another point to be noticed is the effect of fibre size on the radial patterns. It is shown that larger fibres have a much greater tendency than smaller fibres to generate oscillatory radial patterns under the same elastic anisotropy conditions. In this case, the pattern selected by the free energy minimization process, is resisted by the effect of boundary orientation constraints that is in favour of an energy costly mode. This is also the reason why oscillatory patterns will not arise as soon as the elastic constants become different. Instead, the driving force minimizing the free energy due to elastic anisotropy has to overcome the resistance due to the boundary orientation constraint. As the fibre size becomes larger, the effect of such boundary constraints is weakened. Therefore in larger fibres the boundary orientation will have smaller effect on pattern selection, and elastic anisotropy will have a stronger influence. Thus, oscillatory radial patterns will be easier to be observed in larger fibres than in small fibres. As for the non-homeotropic case, in which the boundary orientation is different from the inner boundary orientation, because the pattern consists of a splay–bend mode, the selection of oscillatory patterns would have much less effect on minimizing the free energy than it has on pure bend mode, for the same elastic anisotropy. Therefore, for the same geometric conditions, non-homeotropic boundary orientations would require a stronger elastic anisotropy to induce oscillatory patterns, as shown in the paper.

To determine the stability of any solution, we computed the corresponding second variation of the elastic energy. The oscillatory solutions (PZRi, i = n, h) to the equilibrium equation are shown to be locally stable, whereas the stability of the trivial solution would depend on the ratio of the elastic constants and the ratio of the radii of the outer cylinder and the inner cylinder, as shown by analytical methods.

The interpretation of the numerical results using classical liquid crystal physics leads to explanations of pattern formation phenomena that arise in an industrial process. The elastic anisotropy, which is characterized by the ratio of the two elastic constants $K_1$ and $K_3$, representing the splay and bend deformations, is shown to be the driving force behind the pattern selection mechanism, that leads to the formation of the planar zigzag pattern, frequently observed during fibre spinning.

## Appendix

The objective of this appendix is to present the mathematical analysis that correlates the eigenvalue problem (22) with the bifurcations of equation (9). First we introduce the required non-linear functional analysis concepts. A non-linear mapping $\mathbf{G}$ from a Banach space $\mathbf{H}$ to $\mathbf{K}$ is said to be *Fréchet* differentiable at a point $\upsilon$ provided there is a bounded linear operator $\mathbf{A}$ from $\mathbf{H}$ to $\mathbf{K}$ such that the quantity $R(\upsilon; h) = \mathbf{G}(\upsilon + h) - \mathbf{G}(\upsilon) - \mathbf{A}h$ is $o(h)$ as $h \to 0$; that is

$$\lim_{\|h\| \to 0} \frac{\|R(\upsilon; h)\|}{\|h\|} = 0. \tag{1}$$

We denote by the Fréchet derivative of $\mathbf{G}$ at $\upsilon$ *by* $\mathbf{G}'(\upsilon)$ or by $\mathbf{G}_\phi$; when it exists it may be found by the usual formula of

$$\mathbf{G}'(\upsilon)h = \lim_{t \to 0} \frac{\mathbf{G}(\upsilon + th) - \mathbf{G}(\upsilon)}{t} = \frac{\mathrm{d}}{\mathrm{d}t} \mathbf{G}(\upsilon + th)|_{t=0}. \tag{2}$$

For a non-linear equation,

$$\mathbf{G}(\phi, \mu) = 0 \tag{3}$$

where $\mathbf{G}$ is a differentiable mapping between two Banach spaces $\mathbf{H}$ and $\mathbf{K}$, that is, $\mathbf{G}: \mathbf{H} \times \mathbf{M} \to \mathbf{K}$, where $\mathbf{M}$ is a finite dimensional parameter space. Suppose the operator $\mathbf{G}$ has an equilibrium solution of $(\phi_0, \mu_c)$ at which

$$\mathbf{G}(\phi_0, \mu_c) = 0 \tag{4}$$

Whether the solution $(\phi_0, \mu_c)$ is a bifurcation point is given by the following *Implicit Function Theorem* [21].

*Implicit function theorem 1*

*With the definition of the Banach space* $\mathbf{H}$, $\mathbf{K}$ *and the operator* $\mathbf{G}$ *given above we assume that* $\mathbf{G}$ *is Fréchet dierentiable. The Fréchet derivative of* $\mathbf{G}$ *at* $(\phi_0, \mu_c)$, *designated by* $\mathbf{G}_\phi(\phi_0, \mu_c)$ *is a linear mapping* $\mathbf{G}_\phi : \mathbf{H} \to \mathbf{K}$. *If* $\mathbf{G}_\phi(\phi_0, \mu_c)$ *possesses a bounded inverse, then locally for* $|\mu - \mu_c|$ *sucient small, there exists a dierentiable mapping* $\phi(\mu)$ *from* $\mathbf{M}$ *to* $\mathbf{H}$, *with* $(\phi(\mu), \mu) \subset \mathbf{H} \times \mathbf{M}$, *such that* $\mathbf{G}(\phi(\mu), \mu) = 0$. *Furthermore, in a sucient small neighbourhood of* $(\phi_0, \mu_c)$, $(\phi(\mu), \mu)$ *is the only solution to* $\mathbf{G} = 0$.

From the Implicit Function Theorem, it follows that if $\mathbf{G}$ vanishes at $(\phi_0, \mu_c)$ and $\mathbf{G}_\phi$ is invertible there, then there is a locally smooth curve $\phi(\mu)$ through $(\phi_0, \mu_c)$, and this curve of $\phi(\mu)$ is the unique solution of $\mathbf{G}$ at this point. Therefore a bifurcation can only occur, if the linear mapping of $\mathbf{G}_\phi$, evaluated at $(\phi_0, \mu_c)$, is singular and hence for a linear mapping $\mathbf{A} := \mathbf{G}_\phi(\phi_0, \mu_c) : \mathbf{H} \to \mathbf{K}$ there is no inverse. If the above condition is met, one can conclude that the solution $(\phi_0, \mu_c)$ is a bifurcation point. We rewrite the equation (9) as

$$G(\phi, \mu) = \phi'' - \frac{(-\mu + 1)\sin\phi\cos\phi(1 + \phi'^2)}{\mu\sin^2\phi + \cos^2\phi} = 0 \quad (5)$$

with the boundary conditions

$$\phi(0) = \phi(u_o) = \frac{\pi}{2}. \quad (6)$$

Introducing the linear transformation $\phi = (\pi/2) + \delta$, we have

$$G(\delta, \mu) = \delta'' + \frac{(-\mu + 1)\sin\delta\cos\delta(1 + \delta'^2)}{\mu\cos^2\delta + \sin^2\delta} = 0 \quad (7)$$

with homogeneous boundary conditions

$$\delta(0) = \delta(u_o) = 0. \quad (8)$$

The above equation has a trivial solution of $\delta_0 = 0$, for all values of $\mu$. To examine the stability of the trivial solution $\delta_0$, we shall find values of $\mu$, for which the linear mapping $A = G(\delta_0, \mu)$ does not have an inverse. Hence we must look for the non-trivial solution of the corresponding eigenvalue problem. The linear operator is obtained by taking the Fréchet derivative of (7):

$$A\delta = G_\delta(\delta_0, \mu)\delta = \delta'' - \frac{2(1 + \delta_0'^2)(1 - 2\mu + \mu^2 - \cos(2\delta_0) + \mu^2\cos(2\delta_0))}{(1 + \mu - \cos(2\delta_0) + \mu\cos(2\delta_0))^2}\,\delta. \quad (9)$$

Inserting the trivial solution $\delta_0 = 0$ into this equation, we obtain the linear eigenvalue problem

$$G_\delta(0, \mu)\delta = \delta'' + \left(\frac{1}{\mu} - 1\right)\delta = 0 \quad (10)$$

with the boundary conditions $\delta(0) = \delta(u_o) = 0$. The general solution of the eigenvalue problem is given by

$$\delta(u) = B\cos\left[\left(\frac{1}{\mu} - 1\right)^{1/2} u\right] + D\sin\left[\left(\frac{1}{\mu} - 1\right)^{1/2} u\right]. \quad (11)$$

The boundary condition $\delta(0) = 0$ implies that $B = 0$, so $\delta(u_o) = 0$ gives the eigenvalue $\mu$:

$$\frac{1}{\mu} - 1 = \left(\frac{n\pi}{\Delta u}\right)^2 \quad (12)$$

which gives

$$\mu_{c,n} = \frac{1}{1 + \left(\frac{n\pi}{\Delta u}\right)^2}, \qquad (n = 1, 2, \ldots) \quad (13)$$

and the corresponding eigenfunctions are

$$\delta_n = D_n \sin\left(\frac{n\pi}{\Delta u} u\right), \qquad (n = 1, 2, \ldots). \quad (14)$$

Here $D_n$ are arbitrary constants which cannot be determined from the conditions given above. Now we consider the equation [22]

$$\frac{K_1 - K_3}{2}\delta - \frac{K_1}{2}\delta'' = \lambda\delta \quad (15)$$

which when dividing by $K_1$ gives

$$\delta'' + \left\{\frac{2\lambda}{K_1} - \left(1 - \frac{1}{\mu}\right)\right\}\delta = 0. \quad (16)$$

Since we are looking for $\lambda > 0$, the critical values of $\mu_c$ are to be found by setting $\lambda = 0$. Then the above equation becomes identical to equation (10). So we proved that equation (22) is the Fréchet derivative of equation (9) after the linear transformation (18). Following the Implicit Function Theorem and the discussion, we can now conclude that the branch of the trivial solution ($\delta = 0$, or $\phi = \pi/2$) has multiple bifurcations at the eigenvalues shown above. At the eigenvalues, the linear mapping of $G_\delta$ in (10) becomes singular and doesn't have an inverse. It follows that the non-linear operator of $G$ will have non-trivial solutions in the neighbourhood of $\mu_{c,n}$. At the bifurcation points $\mu_{c,n}$, the non-trivial solution to the linear mapping of $G_\delta$ are the eigenfunctions (14) then we have

$$\phi_n = \delta_n + \frac{\pi}{2} = D_n \sin\left(\frac{n\pi}{\Delta u}\right) + \frac{\pi}{2}, \qquad (n = 1, 2, \ldots). \quad (17)$$

For $n = 1$, $\Delta u = 1$ and $\mu_{c,1} = 0{\cdot}092$, we have the non-

trivial solution of

$$\phi_1 = D_n \sin(\pi u) + \frac{\pi}{2}, \tag{18}$$

which has a half wavelength and matches the numerical solution found at $\mu_{c,1}$. Continuing this process for larger $n$, we find that each eigenfunction matches the numerical solution at that point of $\mu_{c,n}$. Using the Ljapunov–Schmidt method [21], we can decompose $\delta$ in the form

$$\delta = \delta_c + \delta_s \tag{19}$$

where

$$\delta_c = q \sin\left(\frac{n\pi}{\Delta u} u\right) \tag{20}$$

and

$$\delta_s = h(q, u). \tag{21}$$

In (20), $q$ is the amplitude of the oscillatory solution and $h = O(q^2)$ [21].

Linearizing equation (7) and projecting it onto the eigenfunctions, we find

$$\int_0^{u_c} [\delta'' + \lambda(\delta + \delta\delta'^2)] \sin\left(\frac{n\pi}{\Delta u} u\right) \mathrm{d}u = 0. \tag{22}$$

Here $\lambda = ((1/\mu) - 1)$. Substituting (19) into the above integral, we find

$$\int_0^{u_o} \left[ q\left(-\frac{n^2\pi^2}{(\Delta u)^2} + \lambda\right) \sin\left(\frac{n\pi}{\Delta u} u\right) + h'' + \lambda h + \lambda\left(q^3 \frac{n^2\pi^2}{(\Delta u)^2} \sin\left(\frac{n\pi}{\Delta u} u\right) \cos^2\left(\frac{n\pi}{\Delta u} u\right)\right) + o(q^3)\right] \times \sin\left(\frac{n\pi}{\Delta u} u\right) \mathrm{d}u = 0. \tag{23}$$

If we substitute $\lambda = \lambda_n$, the linear terms in $q$ in (23) vanish. Furthermore, since $h$ is orthogonal to the eigenfunctions, we have

$$\int_0^{u_o} (h'' + \lambda h) \sin\left(\frac{n\pi}{\Delta u} u\right) \mathrm{d}u = 0. \tag{24}$$

Therefore, after neglecting higher order terms, the integral (23) becomes

$$\int_0^{u_o} \left[ q\left(-\frac{n^2\pi^2}{(\Delta u)^2} + \lambda\right) \sin\left(\frac{n\pi}{\Delta u} u\right) + \lambda\left(q^3 \frac{n^2\pi^2}{(\Delta u)^2} \sin\left(\frac{n\pi}{\Delta u} u\right) \cos^2\left(\frac{n\pi}{\Delta u} u\right)\right)\right] \times \sin\left(\frac{n\pi}{\Delta u} u\right) \mathrm{d}u = 0. \tag{25}$$

After integrating, we have

$$\frac{q(\lambda - \lambda_n)}{2} - \frac{\lambda}{\lambda_n} \frac{q^3}{4} = 0. \tag{26}$$

Therefore in a small neighbourhood of $\lambda_n$ ($\lambda \approx \lambda_n$), the solution amplitude $q$ and $\lambda$ have the following relationship:

$$q = (2(\lambda - \lambda_n))^{1/2}, \qquad (n = 1, 2, \ldots). \tag{27}$$

Since $\lambda = ((1/\mu) - 1)$, we find that sufficiently close to the bifurcation point, the amplitude $q$ and the elastics anisotropy $\mu$ are related by

$$q = \left(2 \frac{\mu_{c,n} - \mu}{\mu\mu_{c,n}}\right)^{1/2}, \qquad (n = 1, 2, \ldots). \tag{28}$$

Equation (28) predicts that close to a bifurcation of order $n$, the amplitude of the $n$th mode grows at a faster (slower) rate for larger (smaller) $n$. This is in agreement with the numerical results shown in figure 8; by comparing curve A ($n = 1$) with curve C ($n = 3$) we see that the amplitude grows faster in the latter case.

In summary, the contents of this appendix shows the mathematical analysis that explains the multiple bifurcations at eigenvalues. By applying the Ljapunov–Schmidt method [21], we also derive the relationship between the solution amplitude and the elastic anisotropy.



## References


[1] Singer, L. S. 1985, *Faraday Discuss. Chem. Soc.*, **79,** 265.
[2] Edie, D. D., and Dunham, M. G., 1989, *Carbon*, **27,** 647.
[3] Fathollahi, B., and White, J. L., 1994, *J. Rheol.*, **38**, 1591.
[4] Honda, H., 1983, *Mol. Cryst. liq. Cryst.*, **94**, 97.
[5] de Gennes, P. G., and Prost, J., 1993, *The Physics of Liquid Crystals*, 2nd ed. (Oxford: Clarendon).
[6] Pencock, G. M., Taylor, G. H., and FitzGerald, J. D., 1993, *Carbon*, **31,** 591.
[7] Peebles Jr, L. H., 1995, *Carbon Fibers—Formation, Structure, and Properties* (CRC Press, Boca Raton).
[8] Krali, S., and Zumer, S., 1995, *Phys. Rev. E*, 366.
[9] Marroum, R. M., Iannacchione, G. S., Finotello, D., and Lee, M. A., 1995, *Phys. Rev. E*, R2473.
[10] Rey, A. D., 1995, *Phys. Rev. E*, **51**, 6278.
[11] Tsuru, H., 1990, *J. Phys. Soc. Jpn.*, **59,** 1600.
[12] Williams, D. R. M., 1994, *Phys. Rev. E*, **50,** 1686.
[13] Crowford, G. P., Allender, D. W., Doane, J. W., Vilfan, M., and Vilfan, I., 1991, *Phys. Rev. A*, **44,** 2570.
[14] Sokalski, K., and Ruijgrok, Th. W., 1982, *Physica A*, **113,** 126.
[15] Baals, H., and Hess, S., 1988, *Z. Naturf. Teil A*, **43,** 662.
[16] Warmedan, T., Frenkel, D., and Zijlstra, R. J. J., 1987, *J. Phys. (Paris)*, **48,** 319.

[17] Lee, S. D., and Meyer, R. B., 1991, *Liquid Crystallinity in Polymers*, edited by A. Ciferri (New York: VCH), p. 343.
[18] Bird, R. B., Curtis, C. F., Armstrong, R. G., and Hassager, O., 1987, *Dynamics of Polymer Liquids* (New York: Wiley), Vol. 1.
[19] Singh, A. P., and Rey, A. D., 1994, *J. Phys. II (Paris)*, **4,** 645.
[20] Ascher, U. M., Mattheij, R. M., and Russell, R. D., 1988, *Numerical Solution of Boundary Value Problems for Ordinary Differential Equations* (New Jersey: Prentice Hall).
[21] Barbero, G., 1991, *Mol. Cryst. liq. Cryst.*, **195,** 199.
[22] Troger, H., and Steindl, A., 1991, *Nonlinear Stability and Bifurcation Theory* (New York: Springer–Verlag).